

Understanding Structure–Property Relationships under Experimental Conditions for the Optimization of Lithium-Ion Capacitor Anodes based on All-Carbon-Composite Materials

Jinyeon Hwang, Wuyong Zhang, Sol Youk, Konstantin Schutjajew, and Martin Oschatz*

The nanoscale combination of a conductive carbon and a carbon-based material with abundant heteroatoms for battery electrodes is a method to overcome the limitation that the latter has high affinity to alkali metal ions but low electronic conductivity. The synthetic protocol and the individual ratios and structures are important aspects influencing the properties of such multifunctional compounds. Their interplay is, herein, investigated by infiltration of a porous ZnO-templated carbon (ZTC) with nitrogen-rich carbon obtained by condensation of hexaazatriphenylene-hexacarbonitrile (HAT-CN) at 550–1000 °C. The density of lithiophilic sites can be controlled by HAT-CN content and condensation temperature. Lithium storage properties are significantly improved in comparison with those of the individual compounds and their physical mixtures. Depending on the uniformity of the formed composite, loading ratio and condensation temperature have different influence. Most stable operation at high capacity per used monomer is achieved with a slowly dried composite with an HAT-CN:ZTC mass ratio of 4:1, condensed at 550 °C, providing more than 400 mAh g⁻¹ discharge capacity at 0.1 A g⁻¹ and a capacity retention of 72% after 100 cycles of operation at 0.5 A g⁻¹ due to the homogeneity of the composite and high content of lithiophilic sites.

1. Introduction


Ever larger amounts of energy are being consumed globally. In particular, the use of electrical energy is drastically increasing. In many cases, electrical energy must be stored, for example, for the use in small electronic devices, such as laptops or mobile phones, but also for the powering of electric vehicles of the future.^[1–4] Therefore, the development of clean, safe, sustainable, low-cost, and pollution-free electrochemical energy storage systems with fast charging speed, large capacity, and long lifespan is a world-wide goal for the near future.^[5–8]

Among the various electrochemical energy storage systems, electrochemical capacitors (ECs) and Li-ion batteries (LiBs) are dominating the market with a few alternatives getting more and more important.^[9–15] Typical energy densities are EC = 10 Wh kg⁻¹ and LiB = 250–280 Wh kg⁻¹, the power density is EC = 10 kW kg⁻¹, LiB = 1 kW kg⁻¹, and the lifespan ranges from EC = 10⁴ to 10⁵ cycles and LiB = 10³ cycles.^[7,10,15–17] However, the electrochemical mechanisms of energy storage in ECs and LiBs lead to intrinsic limitation of their energy- and power density, respectively. To this end, hybrid Li-ion capacitors (LiCs), which combine the high energy density of LiBs and the high power density and long life span of ECs, emerged as an alternative.^[15–17] By coupling the anode of an LiB and the cathode of an EC, LiCs can possibly combine their advantages and minimize the individual limitations of LiBs and ECs.^[18,19] During cycling, Li-ion storage occurs by a battery-like mechanism (i.e., including at least partial electron transfer) at the anode side and by an EC-like mechanism (i.e., the formation of an electrical-double-layer) at the cathode–electrolyte interface.^[20,21]

The battery-like anode remains the main limitation of LiCs. One widely studied class of materials with high Li storage capacity is carbon-based compounds. To fulfill the requirements for LiCs, carbonaceous anode materials have to provide 1) high electrical conductivity and chemical stability;^[5,7] 2) electronegative heteroatoms such as nitrogen and oxygen that can act as “lithiophilic” sites for strong binding of a large amount of

J. Hwang, Dr. M. Oschatz,^[†]
Institute of Chemistry
University of Potsdam
Karl-Liebknecht-Straße 24–25, Potsdam 14476, Germany
E-mail: Martin.Oschatz@mpikg.mpg.de

W. Zhang, S. Youk, K. Schutjajew, Dr. M. Oschatz
Colloid Chemistry
Max Planck Institute of Colloids and Interfaces
Research Campus Golm, Am Mühlenberg 1, Potsdam 14476, Germany

 The ORCID identification number(s) for the author(s) of this article can be found under <https://doi.org/10.1002/ente.202001054>.

^[†]Present address: Friedrich-Schiller-University Jena, Institute for Technical Chemistry and Environmental Chemistry, Center for Energy and Environmental Chemistry Jena (CEEC Jena), Philosophenweg 7a, Jena 07743, Germany

© 2021 The Authors. Energy Technology published by Wiley-VCH GmbH. This is an open access article under the terms of the Creative Commons Attribution-NonCommercial License, which permits use, distribution and reproduction in any medium, provided the original work is properly cited and is not used for commercial purposes.

DOI: 10.1002/ente.202001054

ions^[11,14]; and 3) a porous structure that ensures rapid transportation of Li ions and accessibility of all lithiophilic sites for cycling at fast rates with low mass transport resistance.^[4,9] To meet these goals, various nitrogen-doped carbon materials and highly porous defective carbon materials were applied, but it remains difficult to combine the properties to provide all the abovementioned properties in one and the same material.^[22–24] For example, the incorporation of large amounts of heteroatoms as well as pores and defects usually decreases electric conductivity. One possible approach to overcome this dilemma is a carbon–carbon composite design.^[25,26] Heteroatom-rich porous carbon with small dimensionality can be engineered into a nanocomposite with a conductive carbon matrix. This approach has been applied recently for sodium-ion capacitor anodes, and it has been shown that ZnO-templated carbon (ZTC) with uniform mesopores and nitrogen-rich carbon synthesized within ZTC host by condensation of hexaazatriphenylene-hexacarbonitrile (HAT-CN)^[27,28] can significantly improve the energy storage capacity and rate capability of the sodium-ion capacitor anode in comparison with the individual compounds or their physical mixture.^[25] The low electrical conductivity of HAT-derived carbon is compensated by the high conductivity of the ZTC matrix, and thus, electron transport and metal storage can be decoupled in such a composite material. Even though this proof-of-principle has been successful, structural characteristics of the materials and the influence of which on the electrochemical characteristics are poorly understood and remain to be optimized. For instance, the loading of nitrogen-rich carbon should be chosen as high as possible to increase the number of ion adsorption sites without significantly decreasing the electrical conductivity of the overall composite too much. It also remains

an open question if comparable effects and conclusions as observed for sodium storage with such composites also hold true for the storage of smaller lithium cations as in LiCs.^[29,30]

To address these questions, a series of all-carbon composite materials with different HAT-CN loading has been synthesized at different temperatures. A fast and a slow drying procedure have been applied to investigate the influence of the homogeneity of the composites. The differences in textural and chemical properties between the samples have been investigated and are linked to the properties of the materials when applied as anode materials for LiCs. It becomes evident that all these “regulation screws” have an important influence on the pore structures and chemical properties of the resulting composite materials. This, in turn, has strong influence on their electrochemical properties.

2. Results and Discussion

Figure 1a shows the procedure to prepare HAT-ZTC composite materials. ZTC was first synthesized through the hard template method using 20 nm-sized ZnO nanoparticles as porogen and sucrose as carbon precursor following a recently reported procedure.^[25] After the heat treatment at 950 °C under inert atmosphere and washing with hydrochloric acid solution, ZTC with a hierarchical micro-mesopore structure was obtained. In the next step, HAT-CN monomers were dissolved in dimethylformamide (DMF) and infiltrated into ZTC at a HAT-CN:ZTC mass ratio of 2:1, 4:1, 6:1, and 8:1, to produce composites denoted as HAT2, HAT4, HAT6, and HAT8, respectively. The influence of the evaporation rate of DMF was studied by applying different drying procedures after mixing. Slowly evaporated composites

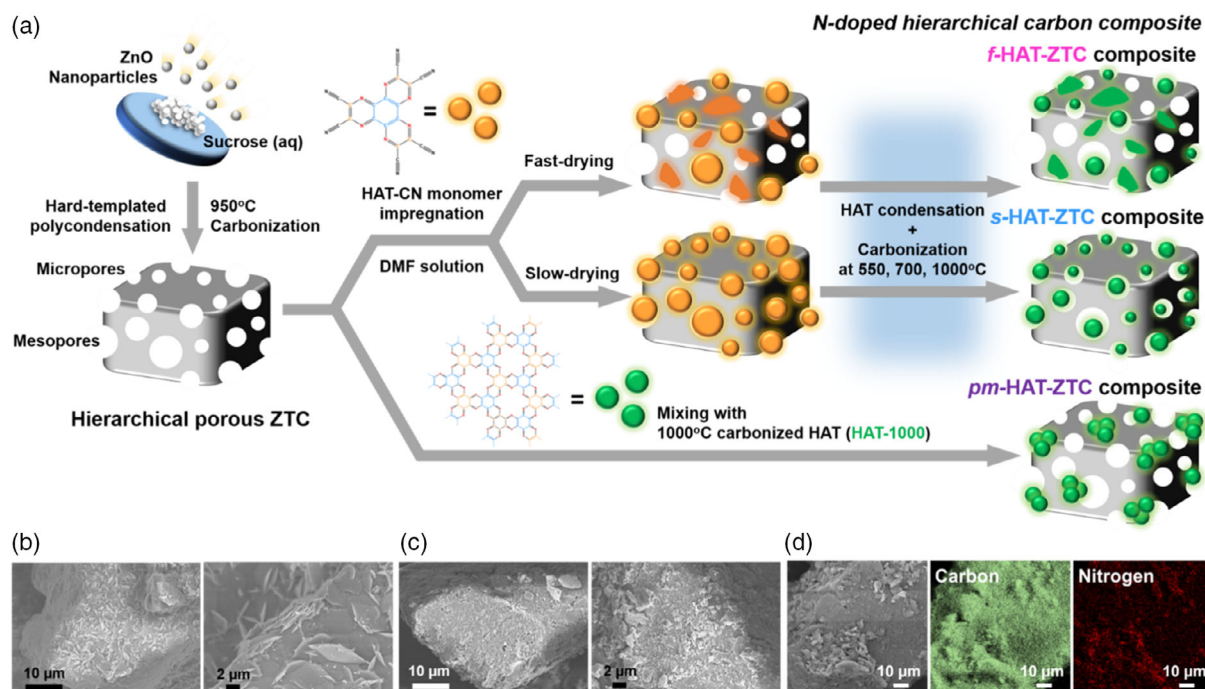


Figure 1. a) Synthesis of HAT-ZTC composites. Depending on the different methods for HAT loading, the materials are denoted as fast-evaporated (f-HAT-ZTC), slow-evaporated (s-HAT-ZTC), and physically mixed (pm-HAT-ZTC) composites. SEM images of b) f-HAT4-550 and c) s-HAT4-550 as well as d) EDS mapping of carbon and nitrogen distribution in f-HAT4-550.

(denoted as “s-HATX”) were dried in a drying oven under air at 60 °C for 2 days first followed by heating in a vacuum oven. On the contrary, the fast evaporated composites (“f-HATX”) were dried directly in the vacuum oven at 60 °C overnight. After infiltration of ZTC with HAT-CN, the latter was condensed through additional heat treatment at 550, 700, or 1000 °C to form HAT-ZTC composite materials. A physically mixed sample (denoted as “pm-HAT-ZTC”) obtained by grinding ZTC and HAT-CN (treated at 1000 °C) in a mortar was also synthesized to investigate the impact of composite formation.

An elemental analysis shown in Table S1, Supporting Information, has been exemplarily performed for composites that underwent fast drying after condensation at different temperatures. Pure ZTC, pure HAT-1000, and pm-HAT-ZTC have been measured for comparison. For a given condensation temperature of f-HATX samples, the nitrogen content is higher in all cases after loading with a higher amount of HAT-CN. In addition, it can be seen that the nitrogen content decreases with increasing condensation temperature, in agreement with previous studies.^[25] Condensation of bulk HAT-CN at 700 °C or below leads to the formation of a C₂N-like material with a high content of pyrazinic nitrogen.^[31–33] In contrast, the material obtained from HAT-CN condensation at 1000 °C is a rather ordinary N-doped carbon with a lower overall nitrogen content, mainly bonded in graphitic structure motives. Thermogravimetric analysis (TGA) curves of the ZTC infiltrated with different amounts of HAT under N₂ and synthetic air atmosphere are shown in Figure S1a, Supporting Information. As ZTC is not losing mass upon heating under inert atmosphere, higher loading with HAT is the reason for higher mass loss during heating up to 1000 °C. Under air, all HAT-loaded ZTCs expectedly show a full mass loss up to ≈700 °C. From the corresponding derivative thermogravimetry curves shown in Figure S1b, Supporting Information, it is shown that the condensation of HAT-CN starting at a temperature slightly above 500 °C is followed by oxidative decomposition and/or depolymerization of the materials slightly below 700 °C. As shown in Figure S1c,d, Supporting Information, the physical mixture, HAT-1000, and the f/s-HAT4-550 composites expectedly show a complete mass loss upon heating to 600–700 °C under synthetic air as well. The physical mixture of polymerized HAT and ZTC as well as HAT-1000 have apparently lower thermal stability in comparison with the composites. The highest temperature necessary for full mass loss is observed in s-HAT4-550, which indicates that there is a difference in structure and resistance against thermal decomposition or oxidation between the composites.

As shown in scanning electron microscopy (SEM) images in Figure 1b,c, f-HAT4-550 has a nonhomogeneous HAT-derived carbon distribution with some disk-like crystals present on the surface of ZTC. Such a morphology is typical for HAT-CN and its condensation products, as shown in Figure S2, Supporting Information. Energy-dispersive X-ray spectroscopy (EDS) mapping shown in Figure 1d confirms a relatively low uniformity of HAT-CN deposition on ZTC after fast drying, as the amount of nitrogen present on the external surface of ZTC shows clear differences between different areas. In contrast, s-HAT4-550 does not contain apparent HAT-like structures on the external surface of the ZTC. This is indicating that unwanted deposition of HAT-CN outside the internal pores of the ZTC host

carbon occurs when the solvent is evaporated fast. Slow drying seems to be crucial to obtain a uniform composite with the HAT-CN uniformly embedded inside ZTC pores.

N₂ physisorption analyses shown in Figure 2a and summarized in Table S2, Supporting Information, result in a type-IV(a) isotherm for pristine ZTC with a high nitrogen uptake below a relative pressure of $p/p_0 = 0.1$ with a constant slope from 0.1 to 0.7, and a hysteresis loop in the range from $p/p_0 = 0.7$ to 1.0. This indicates that a large volume of micropores is combined with mesopores in this material, leading to a high specific surface area (SSA) of 1520 m² g⁻¹ and a total pore volume of 2.55 cm³ g⁻¹. All mesopores seem to be well accessible, as no sign of cavitation can be seen in the isotherm. In contrast, HAT-1000 shows a type-I isotherm, which proves its predominantly microporous structure.^[34] The isotherm of the pm-HAT-ZTC sample lies between that of HAT and ZTC but with low mesopore content resulting from the HAT-1000:ZTC mass ratio of 6:1. As shown in the inset of Figure 2a, the shape of the hysteresis loop of ZTC is fully maintained, revealing that physical mixing of HAT does not affect the pore system of ZTC. Unlike the physical mixture, however, f-HAT and s-HAT composites (data are exemplarily shown for s-HAT4-550 and f-HAT4-550 in Figure 2a) show changed hysteresis loops with signs of cavitation and reduced total pore volume in comparison with the physical mixture. This is a clear sign that the pore structure of ZTC is altered and filled with HAT condensation products. s-HAT4-550 shows a lower total nitrogen uptake and a more significant change of the hysteresis loop in comparison with f-HAT4-550. This confirms that a larger portion of the ZTC mesopores are filled with HAT-derived carbon after slow drying.

These structural differences between the samples are also becoming visible in the differential and cumulative pore distribution curves shown in Figure 2b,c, respectively. In case of pristine ZTC, there is a contribution to the total pore volume coming from micropores below 2 nm as well as from mesopores centered at ≈4 and 10–12 nm. The physical mixture pm-HAT-ZTC has pores in the same size range. A minor but notable contribution to the overall pore volume is still coming from unfilled ZTC pores with the diameters above 10 nm. The pore size distribution of ZTC changes significantly after loading with HAT-CN and its condensation but depends on the applied drying process. In both composites, the micropore volume decreased in comparison with unfilled ZTC. A larger volume of large pores is still present after fast drying. This is again confirming a more homogeneous infiltration of the ZTC pore system with HAT-CN when slow drying is applied. ZTC micropores are apparently all well filled with HAT-CN, but slow solvent removal is crucial for deposition of the precursor molecules for nitrogen-rich carbon inside the larger pores of ZTC instead of deposition on the external surface of the particles. Nitrogen physisorption data of the entire series of prepared composites as well as the condensation products of pure HAT-CN at different temperatures and the corresponding pore size distributions are shown in Figure S3–S10, Supporting Information, and summarized in Figure S11 and Table S2, Supporting Information. The fact that higher condensation temperature of bulk HAT causes an increase in SSA and pore volume is known from previous studies^[27,28] and also becoming obvious in all composite materials independent of the drying method and loading of HAT-CN. This in combination with the lower

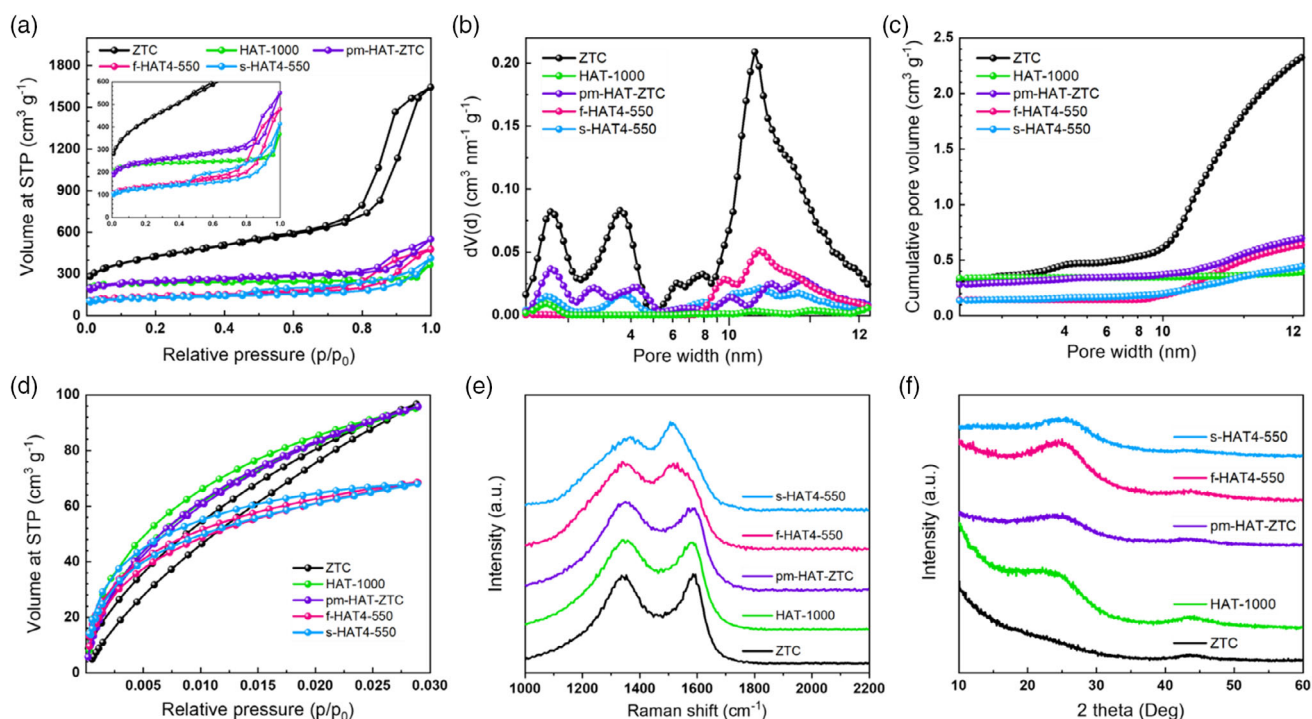


Figure 2. a) N_2 physisorption isotherms (77 K) and corresponding b) differential and c) cumulative pore volume as well as d) CO_2 physisorption isotherms, e) Raman spectra, and f) powder XRD patterns of ZTC, HAT-1000, pm-HAT-ZTC, f-HAT4-550, and s-HAT4-550.

condensation yield at higher temperature (i.e., the higher mass loss of the sample) is responsible for the observed increase in the mass-specific porosity of the composites with a given loading and drying procedure. As another general trend, it presents that the SSA and pore volume of all composites decrease at higher HAT-CN loading at all temperatures applied and for both drying methods. This is reasonable, as the condensation products of HAT-CN have less SSA and pore volume than ZTC, so the corresponding values of the composites decrease at higher content of N-doped carbon. Finally, for all loadings and condensation temperatures, the slow drying method results in composite materials with lower total pore volumes in comparison with the fast drying method. This confirms that a more homogenous pore filling can be achieved with slow drying over a wide range of HAT/ZTC ratios.

CO_2 physisorption isotherms have been measured at 273 K for selected samples as well and are shown in Figure 2d, and Figure S4–S6 and S10, Supporting Information. All nitrogen-doped carbon-containing samples show strong interaction with CO_2 as shown by the high uptake at low relative pressures in the range $p/p_0 = 0 - 0.005$. The total CO_2 uptakes at $p/p_0 = 0.03$ are in line with the micropore volumes detected by nitrogen physisorption measurements. Micropores of ZTC seem to be blocked after loading with HAT-CN and condensation. In all cases, the isotherms are becoming a rather linear shape for materials with lower nitrogen content, that is, with lower HAT-CN loading or with higher condensation temperature. This is caused by the fact that the surface of nitrogen-doped carbons has a stronger interaction with polarizable CO_2 molecules, which can be expected to act as “lithiophilic sites” as well.

Raman spectra are shown in Figure 2e, and Figure S12, Supporting Information. All spectra can still be fitted with a four-band model.^[35] It is becoming obvious that the width of the peaks decreases with lower content of HAT-derived carbon and after condensation at higher temperatures. While condensation at 550 or 700 °C leads to remarkably nitrogen-rich materials with a high content of pyrazinic nitrogen and minor contribution of six-membered carbon rings (responsible for the D-band), ZTC and composites containing HAT-derived carbon condensed at 1000 °C rather show the Raman characteristics of ordinary defect-rich and porous sp^2 -dominated carbon materials with sharper and more intense D-bands but less intense and broadened D_2 - and A-bands. G-bands are shifting toward larger wavenumbers with higher condensation temperature due to the decreasing contribution of C–N bonds and the increasing dominance of C–C bonds. Such materials are expected to have a lower intrinsic affinity to Li ions but at the same time a higher electric conductivity.

Powder X-ray diffractograms have been measured and are shown in Figure 2f, and Figure S13 and S14, Supporting Information. All materials show X-ray diffraction (XRD) curves as typical for highly porous carbon materials without long-range ordering. In some cases, broad reflexes at $\approx 26^\circ$ and $\approx 47^\circ$ can be seen, which are characteristic for stacking into graphite-like domains. Their intensity is, however, not directly representative for the “graphitization” in such a material, as it can be overlaid by scattering intensity from the pore systems at low angles. This scattering intensity is high for ZTC and generally increasing when HAT is carbonized at higher temperatures, which is in line with the physisorption measurements. In all samples where HAT was carbonized at 1000 °C, the (002) reflection at 26° only appears as

shoulder, whereas the (101) reflection at 47° appears relatively sharp. As a clear difference, it shows that the XRD patterns of f-HAT samples are rather similar to bulk HAT-derived carbon materials for a given condensation temperature as compared with the corresponding s-HAT material. This is another indication for the structural differences caused by the chosen drying protocol.

Regarding to the application in LiC anodes, the resistance of composite and cell is of crucial importance as well. This has been experimentally confirmed by measuring electrochemical impedance spectroscopy (EIS). The Nyquist plots displayed in **Figure 3a** elucidate that all composite electrodes have different resistance. Among all samples, s-HAT4-550 has lower intrinsic resistance in comparison with ZTC and other composites.^[36,37] This difference may arise from the uniform carbon coating on the surface of ZTC after slow drying. The nonpolar ZTC surface with lower content of heteroatoms does not have high-energy stabilization sites for Li ions, resulting in inferior interface between electrode and electrolyte. On contrary, HAT containing composites ensure high affinity between Li ions and the electron-donating nitrogen atoms contributing a strong chemical interaction in contrast to rather capacitive Li storage into the pores of ZTC.^[38,39] Homogenous distribution of nitrogen-rich carbon in s-HAT4-550 leads to reduced resistance compared with f-HAT4-550, whereas pm-HAT-ZTC lies between ZTC and HAT-1000.

Full electrochemical characterization of the all-carbon composites and related reference samples has been carried out to conclude on the relationships between their structures and properties as anode materials in LiCs. **Figure 3b** represents the relationship of the irreversible capacities (first irreversible lithiation capacity and the capacity loss by calculating the gap between reversible and irreversible cycles indicated in **Figure S15**, Supporting Information) with the total pore volume and Brunauer–Emmett–Teller (BET) surface area. Larger pore volume and SSA clearly induce an increased portion of irreversible capacity due to the solid-electrolyte interphase (SEI) layer formation, which is proportional to the surface area of the electrode that is accessible for the electrolyte. High surface area ZTC shows a large capacity decay after the first cycle. The changed pore structure and pore filling by composite engineering with N-doped carbon slightly decrease the capacity loss in the composite electrodes. However, even after the composite formation, huge capacity loss is observed which is typical for highly microporous and defect-rich carbons. This disadvantage could possibly be minimized by the use of artificial SEIs or solvent-free electrolytes.^[40,41] Galvanostatic charge–discharge profiles between 0.0 and 3.0 V (vs Li/Li⁺) of a half cell test at a current density of 0.1 A g^{-1} are shown in **Figure 3c**. All curves represent a rather capacitor-like behavior shape dominated by sloping capacity without clear plateaus due to the absence of complete and

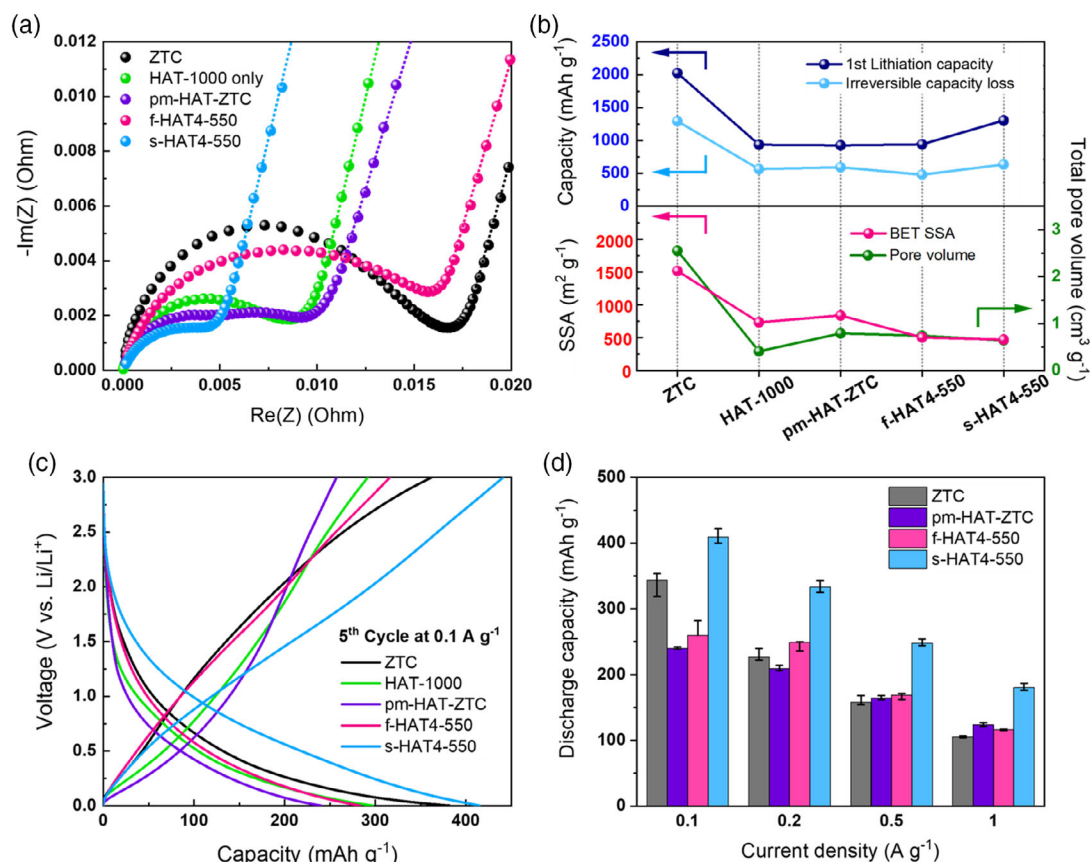


Figure 3. a) Nyquist plots, b) correlation between the first cycle irreversible capacity of LiC and the pores structures, c) charge–discharge voltage profiles (fifth cycle) at 0.1 A g^{-1} , and d) comparison of discharge capacity measured at different current rates (averaged by four cycles each at 0.1, 0.2, 0.5, and 1.0 A g^{-1}) of ZTC, HAT-1000, pm-HAT-ZTC, f-HAT4-550, and s-HAT4-550.

specific electron-transfer processes between electrode and lithium ions. Although ZTC displays the highest capacity at the initial cycling, it degrades rapidly to 381.7 mAh g^{-1} in the fifth cycle. On the other hand, s-HAT4-550 maintains a capacity of 411.2 mAh g^{-1} in the fifth cycle. This is not only significantly higher than the capacity achieved by HAT-1000 and pm-HAT-ZTC, but also exceeds f-HAT4-550. Although the nitrogen-content and chemical bonding motives in both samples are comparable, the intimate contact between both phases and more homogeneous structure of s-HAT4-550 apparently has a significant positive impact on the lithium storage. s-HAT4-550 not only prevails over other materials in terms of capacity, but also in terms of rate capability, as summarized in Figure 3d, and Figure S16, Supporting Information. At 0.1, 0.2, 0.5, and 1.0 A g^{-1} , the averaged discharging capacities are calculated as 409.4, 322.8, 247.8, and 180.2 mAh g^{-1} , respectively.

All capacity data for samples obtained at different temperature, ratio, and drying rate are summarized in Figure S17, Supporting Information. Interestingly, the capacitance does in tendency increase after carbonization at higher temperatures for composites that underwent the fast drying procedure but show different behavior for the slowly dried materials. This could indicate that a redistribution of HAT-derived N-doped carbon takes place at condensation temperatures higher than 550°C . The negative effect of inhomogeneous mixing between ZTC

and HAT-CN after fast drying can, thus, be minimized after condensation at higher temperature.

The rate capability of s-HAT4-550 was investigated in the range from 0.1 to 10 A g^{-1} , as shown in Figure 4a,b. At 2, 5, and 10 A g^{-1} , the averaged specific capacities are 122.4, 57.3, and 27.6 mAh g^{-1} , respectively, with the corresponding coulombic efficiency (C.E.) of 97.9, 96.8, and 96.1%. A long-term cycling test shown in Figure 4c also confirms that s-HAT4-550 has a high reversibility during continuous charging–discharging. Even though the initial capacity of f-HAT6-1000 is higher, it rapidly decayed compared with s-HAT4-550, as shown in Figure S18, Supporting Information. After 100 cycles of operation at 0.5 A g^{-1} , the capacity retention of f-HAT6-1000 is 57%, whereas that of s-HAT4-550 maintains 72% of its initial capacity.

Within such an optimization study, it is also practically important to maximize the capacity per used mass of HAT-CN precursor. In Figure 4d, discharging capacity of all composites measured at 0.1 A g^{-1} divided by the mass of HAT-derived N-doped carbon is plotted versus the condensation yield (including the unchanged mass of ZTC). Among all composites, s-HAT4-550 shows the highest condensation yield and 307.1 mAh g^{-1} of capacity per gram of HAT-derived carbon. For comparison, the yield and capacity per HAT-derived carbon of f-HAT6-1000 are 35.7% and 90.5 mAh g^{-1} , respectively. This is showing the importance of raw material use for the composite

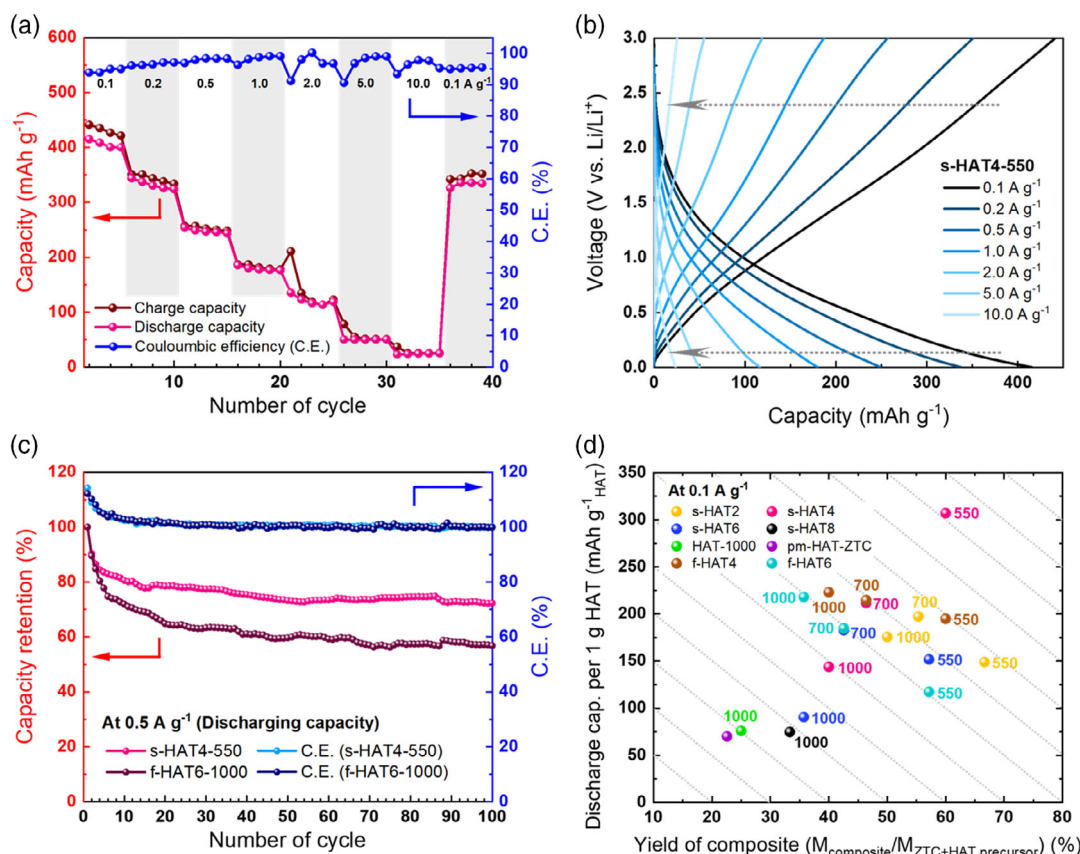


Figure 4. a) Rate capability test of s-HAT4-550 from 0.1 to 10 A g^{-1} , and b) galvanostatic charge–discharge profiles of each current rate. c) Long-term operation result (100 cycles at 0.5 A g^{-1}) of s-HAT4-550 and f-HAT6-1000 with the C.E. and discharging capacity retention compared with the initial capacity. d) Mass-specific discharge capacity of composites per g of HAT-derived N-doped carbon plotted against condensation yield.

design, which is another important aspect that has to be considered in addition to electrochemical data alone.

3. Conclusion

Porous all-carbon composites between ZnO-based hard-templated carbon and nitrogen-containing HAT-CN-derived N-doped carbon were fabricated and applied as anode materials in LiCs. The textures and chemical compositions of the composites are influenced by the loading method and ratio of HAT-CN and by the condensation temperature. Slowly dried s-HAT composites have a more uniform HAT distribution, whereas f-HAT composites that underwent faster drying have a less homogeneous mixing between both compounds. In the latter case, redistribution between HAT-derived N-doped carbon and ZTC can occur after condensation at the temperatures above 550 °C. High nitrogen content and homogenous mixing on the nanoscale improve the adsorptive storage of Li ions at the interface between electrolyte and composite materials. Consequently, the capacity achieved by s-HAT4-550 is superior to the reference materials (ZTC and HAT-1000) and other composites (pm-HAT-ZTC and f-HAT4-550) independent of the chosen current density. These results of this optimization study elucidate the crucial relationship among the LiC cell performance, the textures, and chemical compositions of all-carbon composite materials. Last but not least, we would like to stress out that all the materials discussed here show rather capacitive lithium storage properties without a distinct plateau. Redox-based processes are likely to occur if such materials would be utilized as cathodes in LiBs, and it remains an interesting question, if and how much improvement can be expected when such a hybridization strategy would be applied on the other electrode of the device.

4. Experimental Section

Synthesis of ZTC: ZnO nanoparticles (8.0 g) (20 nm, Nanostructured & Amorphous Materials, Inc.) were mixed with 7 g of sucrose (>99.5%, Sigma-Aldrich) into 13 mL of distilled water. After the formation of a homogeneous dispersion, 0.4 g of powder NaOH was added and stirred. The mixture was then transferred to a petri dish and heated under air at 100 °C for 3 h and then to 160 °C for 6 h to polymerize the sucrose. Samples were then moved to a horizontal tube furnace for carbonization at 950 °C for 2 h under Ar flow with a ramping rate of 1 °C min⁻¹. After cooling, samples were washed at least three times overnight with 1.0 M aqueous HCl solution. Final ZTC materials were filtered and dried at 60 °C in air.

Synthesis of HAT-CN: HAT-CN has been synthesized according to a previously reported procedure.^[42] After mixing of hexaketocyclohexane octahydrate (4 g, 12.6 mmol, Alfa Aesar, 99%) and diaminomaleonitrile (10.88 g, 100.8 mmol, TCI, >96.0%), the mixture was refluxed for 2 h with 150 mL of acetic acid (>99%). The resulting salt was then filtered and washed at least three times with 25 mL of hot acetic acid; 60 mL of nitric acid (30%) was used to suspend black products and heated up to 100 °C for 3 h. When the reaction was finished, the solution was cooled down overnight in ice water. After filtration, obtained particles were refluxed in acetonitrile (400 mL) for 2 h to yield ≈2.3 g of an orange product.

Synthesis of HAT/ZTC Composites: HAT/ZTC composites were prepared by mixing HAT-CN and ZTC powder in inhibitor-free DMF solvent. For HAT2 composites, 350 mg of HAT-CN and 175 mg of ZTC are mixed in 3.0 mL of DMF. For HAT4, 500 mg of HAT-CN was mixed with 125 mg of ZTC, and for HAT6, 600 mg of HAT-CN was mixed with 100 mg of ZTC, and 600 mg of HAT-CN was mixed with 75 mg of ZTC to obtain HAT8. After 1 h of sonication and stirring overnight, the dispersion was moved

into a drying oven at 60 °C under air atmosphere for 2 days. Afterward, composites were moved to a vacuum oven at 60 °C overnight. f-HAT composites have been obtained by the same drying procedure but without the first vacuum-free drying step. After DMF evaporation, mixtures were grinded well and carbonized in the tube furnace at different temperatures (550, 700, and 1000 °C) for 1 h under Ar flow with a ramping rate of 4 °C min⁻¹. Resulting composites are denoted as f- or s-HATX-Y, whereas X represents the mass ratio of HAT divided by ZTC, and Y represents the HAT carbonization temperature. The pm-HAT-ZTC sample was prepared by grinding ZTC and HAT-1000 (HAT-CN carbonized at 1000 °C). The mass ratio between HAT-1000 and ZTC was 6:1.

Characterization: Scanning electron microscopy investigations of the composites have been carried out with a Leo Gemini 1550 (Zeiss), and EDS mapping was performed by X-Max (Oxford instruments) accessorized at the same instrument. The acceleration voltage was 3 kV for SEM images and 10 kV for EDS mapping. TGA was collected using a thermomicrobalance TG 209 F1 Libra (Netzsch) and analyzed by the Proteus (8.0.0) software package. A platinum crucible was used for the measurement in nitrogen or synthetic air (80:20 ratio of N₂:O₂) flow of 20 mL min⁻¹ with a N₂ purge flow of 20 mL min⁻¹ (heating rate = 10 °C min⁻¹). A Quadrasorb apparatus (Quantachrome Instruments) was used to measure N₂ and CO₂ isotherms; 20–40 mg of samples were placed into the 9 mm bulb cell and degassed overnight under vacuum at 135 °C. N₂ physisorption was carried out at 77 K, and CO₂ physisorption was carried out at 273 K. The pore volume was calculated from the nitrogen physisorption isotherms at $p/p_0 = 0.95$, and the SSA was calculated utilizing the multi-point BET model ($p/p_0 = 0.05–0.20$). The quenched-solid density functional theory (QSDFT) was applied to the adsorption branches of the N₂ isotherms to calculate the pore distribution by assuming the carbon pores with a slit/cylindrical shape. X-ray diffraction patterns have been recorded by a D8 (BRUKER) in the 2θ range from 10° to 60° with a scan rate of 0.05° s⁻¹ and a Cu-K_α source ($\lambda = 1.54 \text{ \AA}$). Raman spectra were measured by a Witec Raman Microscope with the 532 nm of green laser at the power of 1.0 mW. The bands are fitted by Gaussian functions.

Electrode Fabrication and Electrochemical Measurements: Before the electrode fabrication, Cu foil (25 μm) was cleaned by acetone and cut into disks of 10 mm in diameter. For the preparation of the electrode ink, 16 mg of active materials, 2 mg of carbon black (Super-P, Alfa Aesar), and 2 mg of sodium carboxymethyl cellulose binder (Sigma, average Mw ≈ 250 000) were mixed in 1.0 mL of Milli-Q water. After making the ink, it was sonicated 1 h and stirred overnight; 30 μL of the final ink was dropped onto the Cu disk, dried at 60 °C in an open oven overnight, and stored in a vacuum oven at 60 °C. The areal loading of the fabricated electrode was between 0.6 and 1.0 mg cm⁻². EIS and charge–discharge half-cell tests were measured with an MPG-2 potentiostat/galvanostat (BioLogic). For all electrochemical cell tests, a Swagelok cell design was adopted. The cell assembly was carried out in an Ar gas filled glove box (H₂O and O₂ level <0.5 ppm) with a Li metal cathode (Sigma, 10 mm disk), Celgard 2320 separator (13 mm disk), and 100 μL of 1.0 M LiPF₆ dissolved in 1:1 (v/v) ethylene carbonate/diethyl carbonate electrolyte. The EIS spectra were measured in two-electrode configuration with lithium metal as a counter electrode at 0 V versus open circuit voltage with a range from 1.0 mHz to 20 kHz at an amplitude of 10 mV. Galvanostatic charge–discharge LiC tests were performed between 0.1 and 10 A g⁻¹ with 0.002–3.0 V cutoff voltage at room temperature.

Supporting Information

Supporting Information is available from the Wiley Online Library or from the author.

Acknowledgements

The authors acknowledge the financial support by the University of Potsdam and the financial support by Max Planck Society in the Fraunhofer-Max Planck collaboration project ClusterBatt.

Open Access funding enabled and organized by Projekt DEAL.

Conflict of Interest

The authors declare no conflict of interest.

Data Availability Statement

Data available on request from the authors.

Keywords

anodes, hybrid materials, nitrogen-doped carbon, porous carbon, lithium-ion capacitors

Received: December 3, 2020

Revised: January 13, 2021

Published online: January 27, 2021

-
- [1] J. W. Choi, D. Aurbach, *Nat. Rev. Mater.* **2016**, *1*, 16013.
- [2] Y. Yang, S. Bremner, C. Menictas, M. Kay, *Renewable Sustainable Energy Rev.* **2018**, *91*, 109.
- [3] Z. P. Cano, D. Banham, S. Ye, A. Hintennach, J. Lu, M. Fowler, Z. Chen, *Nat. Energy* **2018**, *3*, 279.
- [4] H. Shao, Y. C. Wu, Z. Lin, P. L. Taberna, P. Simon, *Chem. Soc. Rev.* **2020**, *49*, 3005.
- [5] J. B. Goodenough, Y. Kim, *Chem. Mater.* **2010**, *22*, 587.
- [6] Y. Liu, Y. Zhu, Y. Cui, *Nat. Energy* **2019**, *4*, 540.
- [7] N. S. Choi, Z. Chen, S. A. Freunberger, X. Ji, Y. K. Sun, K. Amine, G. Yushin, L. F. Nazar, J. Cho, P. G. Bruce, *Angew. Chem., Int. Ed.* **2012**, *51*, 9994.
- [8] L. Borchardt, M. Oschatz, S. Kaskel, *Chem. Eur. J.* **2016**, *22*, 7324.
- [9] L. Borchardt, M. Oschatz, S. Kaskel, *Mater. Horizons* **2014**, *1*, 157.
- [10] V. Etacheri, R. Marom, R. Elazari, G. Salitra, D. Aurbach, *Energy Environ. Sci.* **2011**, *4*, 3243.
- [11] F. Béguin, V. Presser, A. Balducci, E. Frackowiak, *Adv. Mater.* **2014**, *26*, 2219.
- [12] P. Simon, Y. Gogotsi, B. Dunn, *Science* **2014**, *343*, 1210.
- [13] M. Armand, J.-M. Tarascon, *Nature* **2008**, *451*, 652.
- [14] H. Hou, X. Qiu, W. Wei, Y. Zhang, X. Ji, *Adv. Energy Mater.* **2017**, *7*, 1602898.
- [15] H. Wang, C. Zhu, D. Chao, Q. Yan, H. J. Fan, *Adv. Mater.* **2017**, *29*, 1702093.
- [16] D. P. Dubal, O. Ayyad, V. Ruiz, P. Gómez-Romero, *Chem. Soc. Rev.* **2015**, *44*, 1777.
- [17] D. P. Dubal, P. Gómez-Romero, *Mater. Today Energy* **2018**, *8*, 109.
- [18] B. Akinwolemiwa, C. Peng, G. Z. Chen, *J. Electrochem. Soc.* **2015**, *162*, A5054.
- [19] T. Liu, A. A. B. Davijani, J. Sun, S. Chen, S. Kumar, S. W. Lee, *Small* **2016**, *12*, 3423.
- [20] H. S. Choi, T. Kim, J. H. Im, C. R. Park, *Nanotechnology* **2011**, *22*, 405402.
- [21] V. Aravindan, J. Gnanaraj, Y. S. Lee, S. Madhavi, *Chem. Rev.* **2014**, *114*, 11619.
- [22] F. Zhang, T. Zhang, X. Yang, L. Zhang, K. Leng, Y. Huang, Y. Chen, *Energy Environ. Sci.* **2013**, *6*, 1623.
- [23] E. Josef, R. Yan, R. Guterman, M. Oschatz, *ACS Appl. Energy Mater.* **2019**, *2*, 5724.
- [24] L. Chen, R. Yan, M. Oschatz, L. Jiang, M. Antonietti, K. Xiao, *Angew. Chem., Int. Ed.* **2020**, *59*, 9067.
- [25] R. Yan, K. Leus, J. P. Hofmann, M. Antonietti, M. Oschatz, *Nano Energy* **2020**, *67*, 104240.
- [26] M. Perovic, Q. Qin, M. Oschatz, *Adv. Funct. Mater.* **2020**, *30*, 1908371.
- [27] R. Walczak, B. Kurpil, A. Savateev, T. Heil, J. Schmidt, Q. Qin, M. Antonietti, M. Oschatz, *Angew. Chem., Int. Ed.* **2018**, *57*, 10765.
- [28] R. Walczak, A. Savateev, J. Heske, N. V. Tarakina, S. Sahoo, J. D. Epping, T. D. Kühne, B. Kurpil, M. Antonietti, M. Oschatz, *Sustainable Energy Fuels* **2019**, *3*, 2819.
- [29] Y. Li, Y. Lu, P. Adelmhelm, M. M. Titirici, Y. S. Hu, *Chem. Soc. Rev.* **2019**, *48*, 4655.
- [30] P. K. Nayak, L. Yang, W. Brehm, P. Adelmhelm, *Angew. Chem., Int. Ed.* **2018**, *57*, 102.
- [31] J. Mahmood, E. K. Lee, M. Jung, D. Shin, I. Y. Jeon, S. M. Jung, H. J. Choi, J. M. Seo, S. Y. Bae, S. D. Sohn, N. Park, J. H. Oh, H. J. Shin, J. B. Baek, *Nat. Commun.* **2015**, *6*, 4.
- [32] Z. Tian, N. López-Salas, C. Liu, T. Liu, M. Antonietti, *Adv. Sci.* **2020**, *7*, 2001767.
- [33] N. Fechner, N. P. Zussblatt, R. Rothe, R. Schlögl, M. G. Willinger, B. F. Chmelka, M. Antonietti, *Adv. Mater.* **2016**, *28*, 1287.
- [34] M. Thommes, K. Kaneko, A. V. Neimark, J. P. Olivier, F. Rodriguez-Reinoso, J. Rouquerol, K. S. W. Sing, *Pure Appl. Chem.* **2015**, *87*, 1051.
- [35] M. Oschatz, P. Pré, S. Dörfler, W. Nickel, P. Beaunier, J. N. Rouzaud, C. Fischer, E. Brunner, S. Kaskel, *Carbon* **2016**, *105*, 314.
- [36] Z. Xing, Z. Ju, Y. Zhao, J. Wan, Y. Zhu, Y. Qiang, Y. Qian, *Sci. Rep.* **2016**, *6*, 26146.
- [37] D. Bhattacharjya, H. Y. Park, M. S. Kim, H. S. Choi, S. N. Inamdar, J. S. Yu, *Langmuir* **2014**, *30*, 318.
- [38] S. Huang, Z. Li, B. Wang, J. Zhang, Z. Peng, R. Qi, J. Wang, Y. Zhao, *Adv. Funct. Mater.* **2018**, *28*, 1706294.
- [39] A. L. M. Reddy, A. Srivastava, S. R. Gowda, H. Gullapalli, M. Dubey, P. M. Ajayan, *ACS Nano* **2010**, *4*, 6337.
- [40] U. Subramanya, C. Chua, V. G. H. Leong, R. Robinson, G. A. Cruz Cabiltes, P. Singh, B. Yip, A. Bokare, F. Erogbogbo, D. Oh, *RSC Adv.* **2020**, *10*, 674.
- [41] Y. Zheng, Y. Yao, J. Ou, M. Li, D. Luo, H. Dou, Z. Li, K. Amine, A. Yu, Z. Chen, *Chem. Soc. Rev.* **2020**, *49*, 8790.
- [42] B. Kurpil, A. Savateev, V. Papaefthimiou, S. Zafeiratos, T. Heil, S. Özenler, D. Dontsova, M. Antonietti, *Appl. Catal., B* **2017**, *217*, 622.